Pergamon

Int. J. Heat Mass Transfer. Vol. 40, No. 5, pp. 1169–1180, 1997

0017-9310/97 $17.00+0.00

PII: S0017-9310(96)00044-0

Numerical simulation of natural convection of gallium in a narrow gap

R. DEREBAIL and J. N. KOSTER†

University of Colorado, Department of Aerospace Engineering Sciences, Boulder, CO 80309-0429, U.S.A.

(*Received* 20 *November* 1995 *and in final form* 30 *January* 1996)

Abstract—Natural convection in a low Prandtl number, liquid metal gallium was numerically simulated in a 2 mm narrow gap test cell to benchmark experiments. One two-dimensional model and three different three-dimensional models were tested using a commercial finite element code and compared to an X-ray visualization experiment. Significant differences were found between the results obtained in the two-dimensional and individual three-dimensional models. The inclusion of the bounding solid walls of the test cell in the three-dimensional model resulted in temperature contour profiles which are comparable to the experimental visualization in liquid gallium. Copyright © 1996 Elsevier Science Ltd.

1. INTRODUCTION

In a natural convection fluid flow experiment a horizontal temperature gradient is imposed on a fluid layer of gallium. Gallium is a low Prandtl number ($Pr = 0.027$) metal and has a melting point of 29.78°C. Recently a new, noninvasive, *in situ* radioscopic method of liquid metal flow visualization has been developed. This technique uses a real time X-ray radioscopy system and has been employed to visualize particle flow and the morphology of melting and solidification interfaces [1–7]. Density and temperature fields were visualized during natural convection of liquid gallium in a narrow gap test cell.

Stewart and Weinberg [8, 9] investigated both numerically (two-dimensional) and experimentally the effect of buoyancy induced flow on the temperature distribution and heat transfer in a rectangular enclosure filled with liquid tin. The two-dimensional model did not estimate accurately the experimental natural convection flow and heat transfer in a three-dimensional cavity. In addition, the temperature profiles were estimated by the authors using radioactive tracers and by performing autoradiography on the quenched solid.

Viskanta *et al.* [10] described a three-dimensional numerical model for natural convection in a liquid metal ($Pr = 0.02$) filled cavity and compared their results to experimental data. Wolff *et al.* [11] reported a combined experimental and two-dimensional numerical study of natural convection heat transfer and fluid flow in vertical cavities filled with liquid metals. Their numerical results did not match the experimental temperature measurements, in particular at the center of the cavity. In both these papers a crude finite difference grid and a wide gap cavity (width ~38 mm) were used. Viskanta *et al.* [10] concluded that their three-dimensional calculations were preliminary and needed a better mesh refinement and a larger mesh to get a good match of their results. Wolff *et al.* [11] emphasized the need for highly accurate three-dimensional numerical simulations.

The main motivation for this paper is to numerically simulate temperature flow fields in a test cell used for natural convection experiments in liquid gallium. The second motivation for this paper is to provide accurate three-dimensional numerical simulations in low Prandtl number liquid metals and to compare to experimental results obtained via the non-intrusive X-ray radioscopy technique described in Koster *et al.* [7].

2. EXPERIMENTAL SETUP

The experimental test cell is described in detail by Koster *et al.* [7]. The test cell was made of Plexiglas. The gallium filled cavity had a width of 2 mm. Such a narrow gap guarantees a steady-state convective flow up to very high Grashof numbers. An adjustable lid made of Plexiglas was inserted into the cavity to provide a rigid upper surface on the liquid metal and also to fix the aspect ratio of the liquid metal in the test cell. Lateral thermodes are made of molybdenum-cladded copper and have a recirculating flow channel through which the heating/cooling fluid flows. The top, bottom, front and back walls were thermally insulated with radiographically transparent plastic insulation. Plexiglas provides adiabatic thermal boundary conditions. Copper thermodes can be considered perfectly conducting at the molybdenum plates. Molybdenum plates have only four times higher thermal conductivity than gallium (refer to Table 1) and there-

† Author to whom correspondence should be addressed.

NOMENCLATURE

A aspect ratio, $A = L/H$
c_p specific heat
d width of cavity
$\mathbf{g}$ gravitational acceleration
Gr Grashof number
h heat transfer coefficient
H height of cavity
k thermal conductivity
L length of cavity
n total number of nodal points at the cold or hot wall
Nu Nusselt number
Nu_{av} average Nusselt number
Nu_{local} local Nusselt number
p pressure
p^* dimensionless pressure
q heat flux
Pr Prandtl number
$R(\mathbf{u}_i)$ residual vector
Ra Rayleigh number
T temperature
T^* dimensionless temperature
$\mathbf{u}$ velocity vector, $\mathbf{u} = \{u, v, w\}$
$\mathbf{u}_i$ solution vector
u, v, w velocities in the x, y and z coordinates, respectively
u^*, v^*, w^* dimensionless velocities in x, y and z coordinates, respectively
x, y, z coordinates
x^*, y^*, z^* dimensionless coordinates.

Greek symbols
β coefficient of thermal expansion
γ ratio of solid to melt thermal conductivity
ΔT temperature gradient
κ thermal diffusivity
μ dynamic viscosity
ν kinematic viscosity
ρ density.

Subscripts
c cold
h hot
i iteration number
0 refers to reference state.

Superscripts
m melt
s solid.

Table 1. Properties of gallium, Plexiglas, molybdenum and copper

Parameter	Symbol	Value	Units	References
	Gallium			
Melting point	T_m	29.78	°C	[12]
Volumetric coefficient of thermal expansion	β(373 K)	1.2×10^{-4}	K^{-1}	[12]
Viscosity	μ	2.04×10^{-3}	$kg\,m^{-1}\,s^{-1}$	[13]
Density	ρ^m (302.78 K)	6094.70	$kg\,m^{-3}$	[12]
Thermal conductivity	k^m (302.78 K)	28.68	$W\,m^{-1}\,K^{-1}$	[12]
Specific heat	c_p (500 K)	384.7	$J\,kg^{-1}\,K^{-1}$	[12]
	Plexiglas			
Density	ρ^s (293 K)	1190	$kg\,m^{-3}$	[14]
Thermal conductivity	k^s (293 K)	0.20	$W\,m^{-1}\,K^{-1}$	[14]
Specific heat	c_p (293 K)	1466	$J\,kg^{-1}\,K^{-1}$	[14]
	Molybdenum			
Density (293 K)	ρ^s (293 K)	10200	$kg\,m^{-3}$	[15]
Thermal conductivity	k^s (298.2 K)	138	$W\,m^{-1}\,K^{-1}$	[15]
Specific heat	c_p (298 K)	249.95	$J\,kg^{-1}\,K^{-1}$	[15]
	Copper			
Thermal conductivity	k^s (298.2 K)	393.98	$W\,m^{-1}\,K^{-1}$	[15]

fore do not provide a perfect conducting boundary condition at the interface with liquid gallium.

3. NUMERICAL MODEL

Figure 1(a) shows the three-dimensional sketch of the model used for numerical simulation of the natural convection test cell containing gallium. The overall dimensions of the Plexiglas test cell are $50 \times 57 \times 38$ mm. The top, bottom, front and back side of the gallium cavity are surrounded by Plexiglas walls and included in one three-dimensional model. The front and back walls have dimensions of $50 \times 42 \times 18$ mm, the bottom wall has dimensions of $50 \times 15 \times 38$ mm and the top wall has dimensions of $50 \times 7 \times 2$ mm. The central three-dimensional cavity has dimensions of $50 \times 35 \times 2$ mm ($L \times H \times d$) and is filled with pure gallium. The molybdenum plates on the thermodes are included as solid walls in the model. The dimensions of the molybdenum plates are $1 \times 46 \times 12$ mm. Figure 1(b) is the sketch of the cavity containing the gallium melt. The cavity is differentially heated from the sides, with the left wall being the cold wall and the right wall being the hot wall.

4. MATHEMATICAL FORMULATION

The flow field and temperature distribution is governed by the Navier–Stokes and energy equations. The governing Navier–Stokes equations, expressing conservation of mass, momentum and energy in the gallium melt, were nondimensionalized using the following variables:

$$x^* = \frac{x}{H} \quad y^* = \frac{y}{H} \quad z^* = \frac{z}{H} \quad u^* = \frac{u}{\left(\frac{\kappa^m}{H}\right)} \quad v^* = \frac{v}{\left(\frac{\kappa^m}{H}\right)}$$

$$w^* = \frac{w}{\left(\frac{\kappa^m}{H}\right)} \quad p^* = \frac{p}{\rho^m\left(\frac{\kappa^m}{H}\right)^2} \quad T^* = \frac{T-T_c}{T_h-T_c}. \tag{1}$$

The Boussinesq approximation, in which density is constant everywhere except in the gravitational force term, is applied to the momentum equation. This equation is written as follows:

$$\rho = \rho_0[1-\beta(T-T_0)]. \tag{2}$$

The Rayleigh number (Ra), Prandtl number (Pr), and Grashof numbers (Gr), are defined as follows:

$$Ra = \frac{g\beta\frac{(T_h-T_c)}{L}H^4}{\nu\kappa^m} \tag{3}$$

$$Pr = \frac{\nu}{\kappa^m} \tag{4}$$

$$Gr = \frac{g\beta\frac{(T_h-T_c)}{L}H^4}{\nu^2}. \tag{5}$$

Therefore the dimensionless governing equations of conservation of mass, momentum and energy are written as (after dropping the * superscript):

$$\nabla\cdot u = 0 \tag{6}$$

$$\mathbf{u}\cdot\nabla u = -\nabla p + Pr\nabla^2 u \tag{7}$$

$$\mathbf{u}\cdot\nabla v = -\nabla p + Pr\nabla^2 v \tag{8}$$

$$\mathbf{u}\cdot\nabla w = -\nabla p + ARaPrT + Pr\nabla^2 w \tag{9}$$

$$\mathbf{u}\cdot\nabla T = \nabla^2 T. \tag{10}$$

The Plexiglas walls and the molybdenum walls are solid entities within the model and therefore must have their energy equation solved. Since the walls are motionless, the energy equation can be written as follows:

$$\kappa^s\nabla^2 T = 0 \tag{11}$$

where κ^s is the thermal diffusivity of the solid entity (either Plexiglas or molybdenum depending upon the wall in consideration). Taking the same scaling factors as those used in the governing equations for the melt, we obtain the following non-dimensionalized energy equation for the solid walls

$$\nabla^2 T = 0. \tag{12}$$

No-slip velocity boundary conditions are imposed at the top, bottom, front and back rigid walls. These four walls have finite thermal conductivity properties. The boundary conditions for the outer molybdenum hot and cold walls are

$$\mathbf{u} = 0 \quad T = T_c \quad \text{at } x = -1 \text{ mm} \quad \forall y, \forall z$$

$$\mathbf{u} = 0 \quad T = T_h \quad \text{at } x = L+1 \text{ mm} \quad \forall y, \forall z. \tag{13}$$

Perfect thermal contact is assumed at the melt/molybdenum interface and the melt/Plexiglas interface, so that the conductive fluxes at this boundary are equal. From the general heat transfer equation,

$$q = k\frac{dT}{dx} \tag{14}$$

we may equate the thermal fluxes as

$$q^m = q^s \tag{15}$$

which when nondimensionalized yields

$$q^m = \gamma q^s \tag{16}$$

where $\gamma = k^s/k^m$ the ratio of the thermal conductivities of the solid wall (either molybdenum or Plexiglas) to that of the gallium melt.

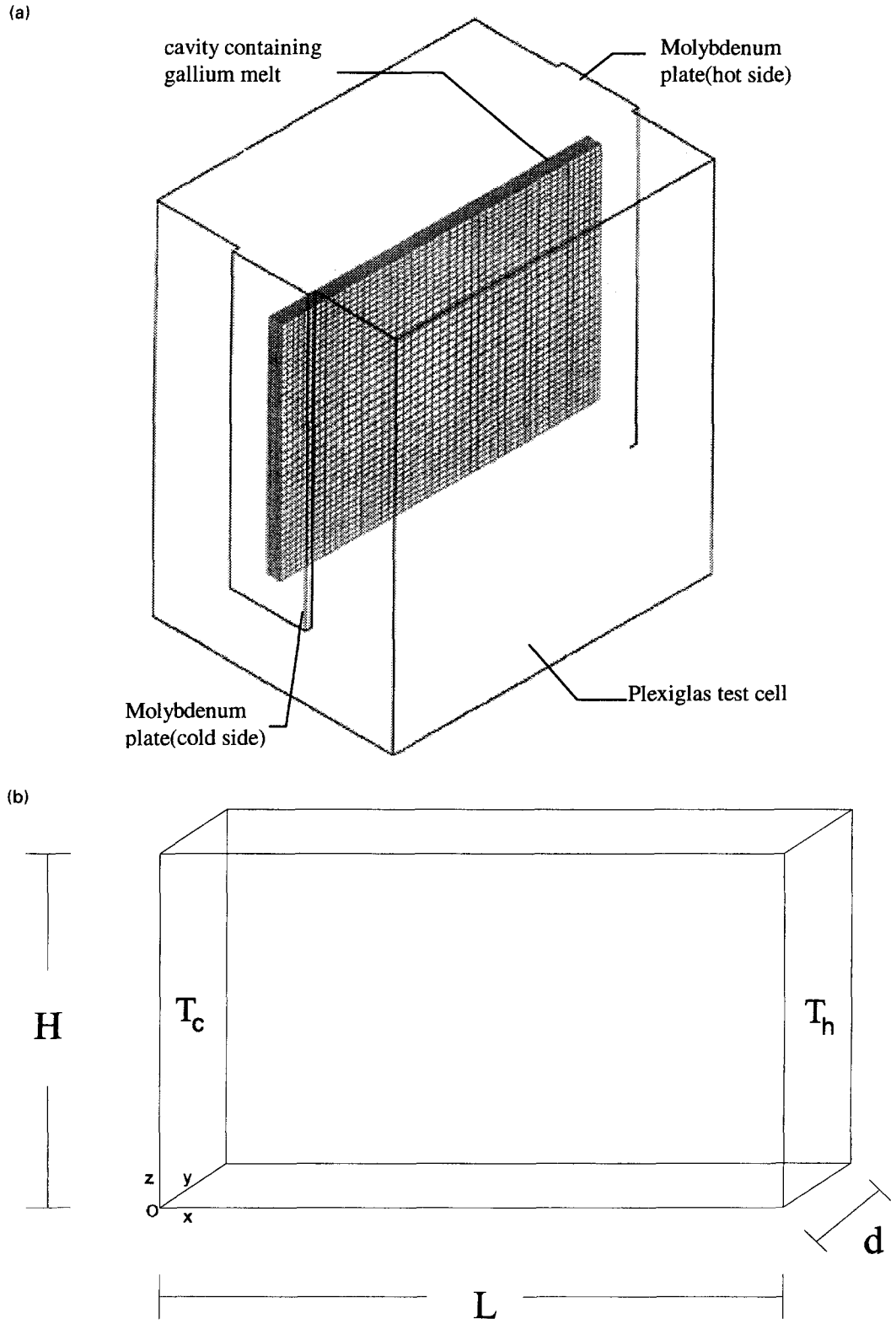

Fig. 1. (a) Sketch of model used for numerical simulation. (b) Three-dimensional fluid cavity.

5. NUMERICAL SOLUTION

Four different models were tested and these are listed in Table 2. First a two-dimensional model was tested. This model was then extended to a three-dimensional cavity. The first three-dimensional model considered the fluid only, with idealized adiabatic and perfectly conducting boundary conditions. The second three-dimensional model considered the fluid and the Plexiglas front and back walls. Finally, a complete three-dimensional model was tested which considered all the components of the experimental test cell, which includes the four Plexiglas walls and two molybdenum side walls. Discussions in the Mathematical Formulation section and this section will refer to three-dimensional Model III, which is the most complicated and complete model.

The flow is assumed to be steady, laminar, incompressible and three-dimensional. The nonlinear governing equations are discretized and solved numerically by using the finite element code FIDAP (Release 7.51). FIDAP uses the conventional finite element Galerkin formulation [16]. Test runs with time-dependent governing equations were performed for three-dimensional Model I using FIDAP at a $\Delta T = 50$ K. The largest change in the maximum velocity between successive time steps was 1.3%, while that of the maximum pressure was 0.05%. With further increase in time, this change in maximum velocity and maximum pressure decreased to less than 0.001%. These results proved our assumption of steady-state solution in a narrow gap to be true. This allowed us to use the faster steady-state governing equations for further analysis.

Eight-node continuum brick elements are employed for the discretization of temperature and velocity. A graded mesh with $50 \times 23 \times 55$ grid points in the x, y and z directions is used. The model includes the liquid layer, molybdenum walls and Plexiglas walls. The liquid layer itself is modeled with $50 \times 11 \times 41$ grid points in the x, y and z directions ($50 \times 2 \times 35$ mm^3 liquid volume). In all four models, a nonuniform gridding scheme was used; with more elements at the edges of the cavity than at the center of the cavity. The properties used in the numerical model for the liquid gallium, Plexiglas test cell walls, and molybdenum walls are listed in Table 1.

Grid tests were performed for all four models with the maximum velocity and maximum stream function as parameters for comparison. For the two-dimensional model, a grid resolution was chosen which was sufficient and does not have an effect on the solution. For the three-dimensional models, we chose a grid resolution which is sufficient for the accuracy of the solutions obtained, but approaches the limits of our computer resources. Some of the post-processing was done with Corel Photo Paint, Microsoft Excel and Sigma Plot software.

Convergence of the numerical calculations is achieved whenever the following criteria are satisfied:

$$\frac{\| \mathbf{u}_i - \mathbf{u}_{i-1} \|}{\| \mathbf{u}_{i-1} \|} \leqslant 10^{-3} \tag{17}$$

$$\frac{\| \mathbf{R}(\mathbf{u}_i) \|}{\| \mathbf{R}_0 \|} \leqslant 10^{-3} \tag{18}$$

where $\| \cdot \|$ is the Euclidean norm, $\mathbf{u}_i$ is the solution vector, and $R(\mathbf{u}_i)$ is the residual vector (i indicates the ith iteration). Because both $\nabla \mathbf{u}_i$ and $R(\mathbf{u})$ tend to zero near the real solution, a combination of these two criteria provides a sufficient and effective overall convergence criterion for all possible situations.

Nonlinear solutions were obtained by using a Segregated Solver [16]. The solution strategy for this three-dimensional problem was to perform one or two iterations with the successive substitution solution algorithm and then switching to the segregated solver solution algorithm. The strategy of using the slower, but more robust successive substitution method in the early phase of calculations was to bring the solution within the radius of convergence of the faster converging segregated solver method.

6. HEAT TRANSFER

The heat transfer rate by convection can be best described by the Nusselt number at the vertical walls. Nusselt number is the ratio of the heat transferred by convection to the heat transferred by conduction. The Nusselt number (Nu) is defined as

$$Nu = \frac{hL}{k^{\mathrm{m}}}. \tag{19}$$

Hauf and Grigull [17] presented a modified equation to calculate the local Nusselt number at a wall in a differentially side-wall heated cavity based on the

Table 2. List of different numerical models tested

Model	Configuration	Mesh size: Overall	Mesh size: Fluid layer
Two-dimensional model	Fluid only	91×63	91×63
Three-dimensional Model I	Fluid only	$71 \times 11 \times 51$	$71 \times 11 \times 51$
Three-dimensional Model II	Fluid; front and back Plexiglas walls	$71 \times 21 \times 51$	$71 \times 11 \times 51$
Three-dimensional Model III	Fluid; front, back, top and bottom Plexiglas walls; hot and cold molybdenum walls	$59 \times 23 \times 55$	$51 \times 11 \times 41$

slope of the temperature distribution curve. The equation can be rewritten as follows:

$$Nu_{\text{local}} = \left(\frac{\partial T}{\partial x}\right)_{\text{wall}} \frac{L}{\Delta T}, \tag{20}$$

where $(\partial T/\partial x)_{\text{wall}}$ is the temperature slope at the wall, L is the length of the cavity across which a temperature gradient of ΔT is applied.

The average Nusselt number (Nu_{av}) can then be obtained by averaging the local Nusselt number over all the nodes at either the hot or cold wall. This equation can be written as follows:

$$Nu_{\text{av}} = \frac{\sum_{\text{nodes}} Nu_{\text{local}}}{n}, \tag{21}$$

where n is the total number of nodal points at the wall.

Figure 2 is a plot of the average Nusselt number vs the Grashof number calculated at the cold wall for the two-dimensional model and three-dimensional Model I. For the two-dimensional model the average Nusselt number at the cold wall was obtained by averaging the local Nusselt number at 63 nodal points, while in the three-dimensional Model I the averaging was done over a two-dimensional surface consisting of 561 nodal points. In the two-dimensional case, up to a Grashof number of 10^6, the Nusselt number increases rapidly by convection and then slows down with further increase in Grashof number. However in the case of the three-dimensional model, the Nusselt number increases almost linearly with increase in Grashof number. It should also be noted that for the same Grashof number, the Nusselt number is lower in the three-dimensional case compared to the two-dimensional case.

Table Curve® two-dimensional software was used to obtain a correlation between the average Nusselt number (Nu_{av}) and the Grashof number (Gr) by curve fitting. Equations (22) and (23) are the correlations obtained for the two- and three-dimensional Model I, respectively.

Two-dimensional model:

$$Nu_{\text{av}} = 0.083 + 0.052 Gr^{0.293} \tag{22}$$

Three-dimensional Model I:

$$Nu_{\text{av}} = 0.882 + 9.312 \times 10^{-7} Gr^{0.909}. \tag{23}$$

Figure 2 shows that the average Nusselt number vs the Grashof number relationship is almost linear for three-dimensional Model I. Therefore equation (23) can be replaced by a linear correlation shown below in equation (24).

Three-dimensional Model I:

$$Nu_{\text{av}} = 1 + 2 \times 10^{-7} Gr. \tag{24}$$

7. TEMPERATURE FIELD VISUALIZATIONS

Figure 3 is a velocity vector plot in the fluid from the central plane of the three-dimensional Model III for a Grashof number of 18.9×10^6. Here the right side is the hot end, while the left side is the cold end. We see that there is a single roll cell rotating in the counter clockwise direction as expected for natural convection. As the main goal of our simulations is the comparison with experimentally visualized density

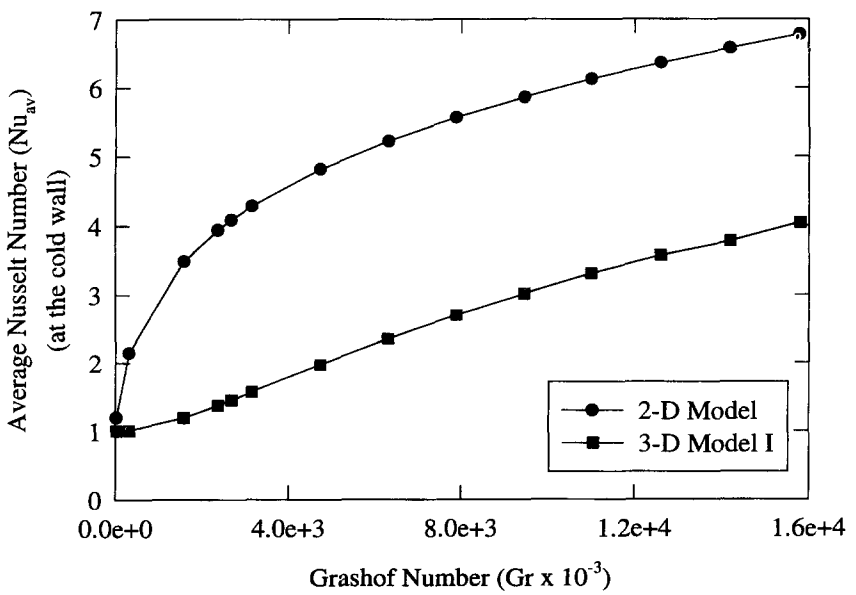

Fig. 2. Average Nusselt number at the cold wall vs the Grashof number for the two-dimensional model and three-dimensional Model I.

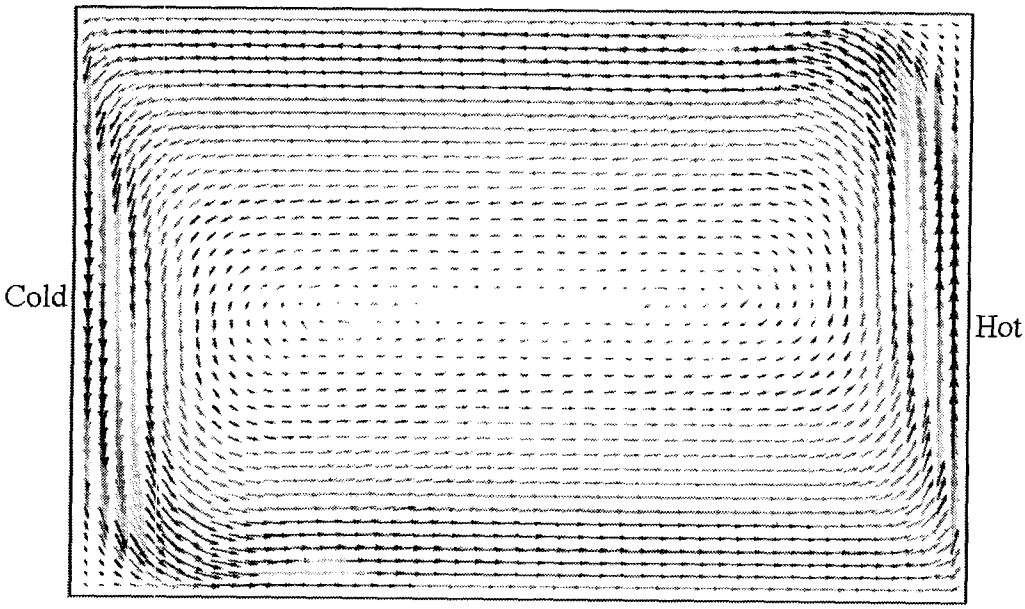

Fig. 3. Velocity vector plot of the central plane from three-dimensional Model III.

and temperature fields, we will focus hereafter on temperature plots.

Figure 4(a, b) shows the nondimensional temperature contour plots obtained for different Grashof numbers for the two-dimensional model and the three-dimensional Model I, respectively. As the Grashof number increases, the temperature isotherms tend to flatten out gradually. Hot fluid is moving upwards at the right side wall and downward at the cold wall. It can be seen that there are significant differences in the contours between two-dimensional and idealized three-dimensional model (wherein the front, back, bottom and top walls are adiabatic; the heated side walls are perfectly conducting.) For three-dimensional Model I, we have plotted the temperature contour in the central plane of the fluid. From the plots it is apparent that for all Grashof numbers the temperature contours are almost completely different between the two models. In the two-dimensional model, the isotherms seem to bend downward and then back upward close to the cold wall and *vice versa* at the hot wall. However in the case of the three-dimensional Model I no such trend was noticed. These differences confirm that two-dimensional models cannot really be used for comparison to three-dimensional experiments, except maybe to obtain an initial approximation for an assessment of the underlying physics.

In a next refinement, the front and back Plexiglas walls were added to the three-dimensional model. In the actual experiment, the front and back walls were made of Plexiglas and had a finite thermal conductivity. The ratio of thermal conductivity between the melt and the Plexiglas is $k^m/k^s \sim 140$. A finite conductivity will result in heat losses through the solid walls. Three-dimensional Model II included the solid walls as an entity within the model, perfect thermal contact was assumed at the melt/Plexiglas interface and the conductive fluxes at this boundary were set to be equal. At the outer boundary of the Plexiglas, the boundary condition is set to adiabatic.

Figure 5(a, b) shows the averaged nondimensional temperature contours for three-dimensional Model I and three-dimensional Model II at $Gr = 15.8 \times 10^6$, respectively. The average temperature contours are calculated by averaging the temperatures across 11 planes in the melt for three-dimensional Model I and for three-dimensional Model II. In the actual experiment the image that we obtain is an integrated image along the radiation path. Therefore in order to compare numerical models to the experimental results the temperatures across the vertical planes of the numerical models were averaged. It can be seen that the temperature contours are steeper in the three-dimensional Model II with solid walls than those in three-dimensional Model I with melt and adiabatic walls.

Although there are differences between the temperature contours for the two three-dimensional models as shown in Fig. 5(a, b), these differences are not clearly apparent on looking at the plots. Therefore in order to illustrate these differences clearly, we have plotted the average nondimensional temperatures at $z^* = 1.0$ and $Gr = 15.8 \times 10^6$ for the three-dimensional Model I vs three-dimensional Model II in Fig. 5(c). If this plot is a straight line, then there are no differences between the two three-dimensional models. However Fig. 5(c) is not a straight line and therefore the three-dimensional Model I differs from three-dimensional Model II. Although the differences are minor, solid walls cannot necessarily be neglected.

Our next step was to include all the solid walls in our three-dimensional Model III. In addition to the

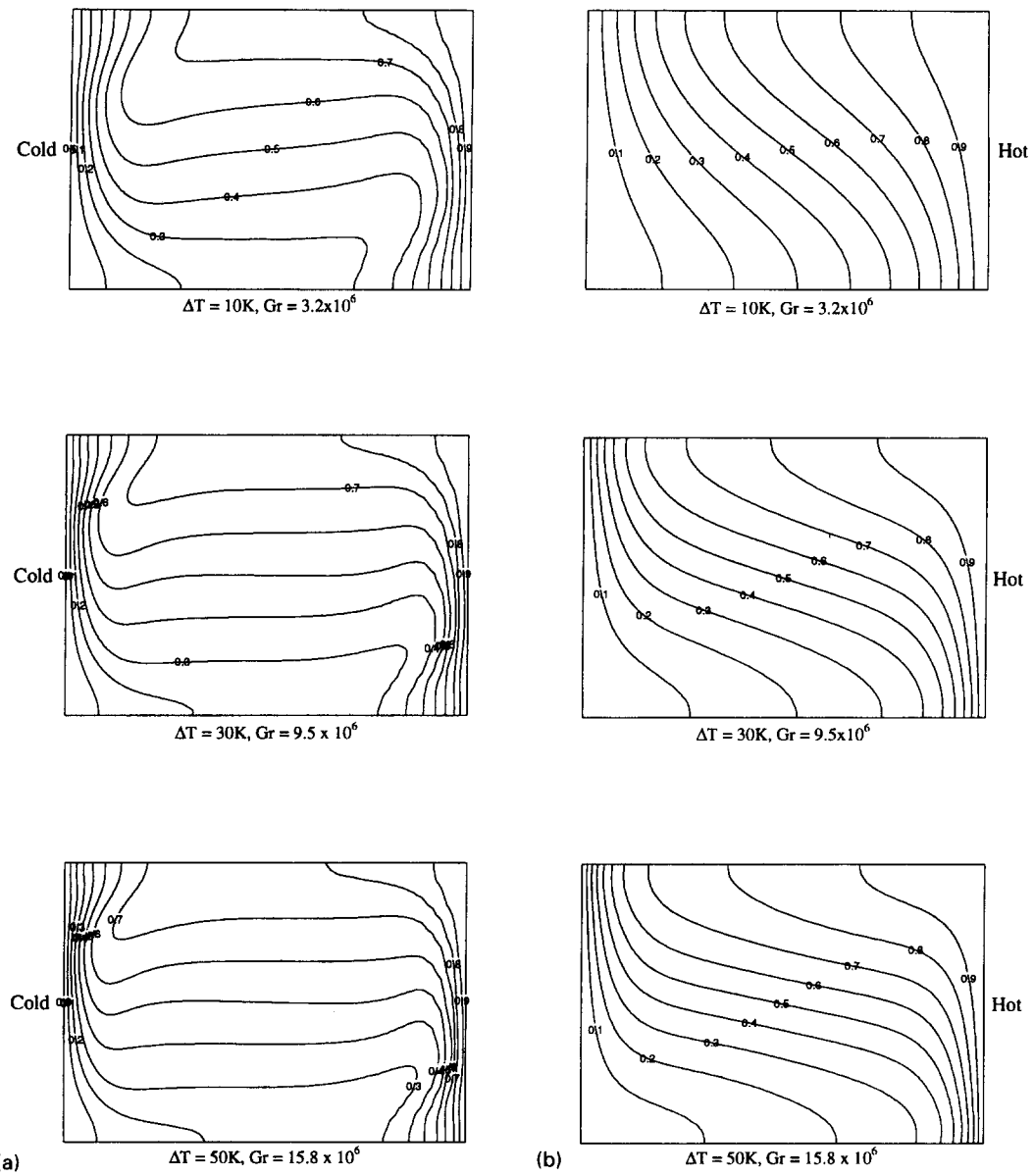

Fig. 4. Nondimensional temperature contours. (a) Two-dimensional model. (b) Central plane in the test cell for three-dimensional Model I.

Plexiglas front, back, top and bottom walls, we also included the molybdenum hot and cold walls. The copper thermodes are considered perfectly conducting. Once again perfect thermal contact was assumed at the melt/molybdenum interface, so that the conductive fluxes at this boundary are equal. The three-dimensional Model III is believed to be the closest approximation to the actual experimental test cell. Figure 6(a, b) shows the average nondimensionless temperature contours for three-dimensional Model I and three-dimensional Model III at $Gr = 15.8 \times 10^6$, respectively. The average temperature contours are calculated by averaging the temperatures across 11 planes for three-dimensional Model I and for three-dimensional Model III. Compared to the three-dimensional Model I the temperature contours for the three-dimensional Model III tend to flatten out at the center of the test cell at higher Grashof numbers.

Figure 6(c) is a plot which compares the average temperature contours at $z^* = 1.0$ and $Gr = 15.8 \times 10^6$ for the three-dimensional Model I with that of three-dimensional Model III. This plot clearly illustrates the magnitude of the deviation in the average temperatures at a particular location, with and without the inclusion of the solid walls of the test cell. This deviation is much larger than the expected deviation shown in Fig. 5(c), since the three-dimensional Model II only includes two walls, whereas in the three-dimensional Model III all six surrounding walls are included.

Figure 7(a, b) shows the nondimensional tem-

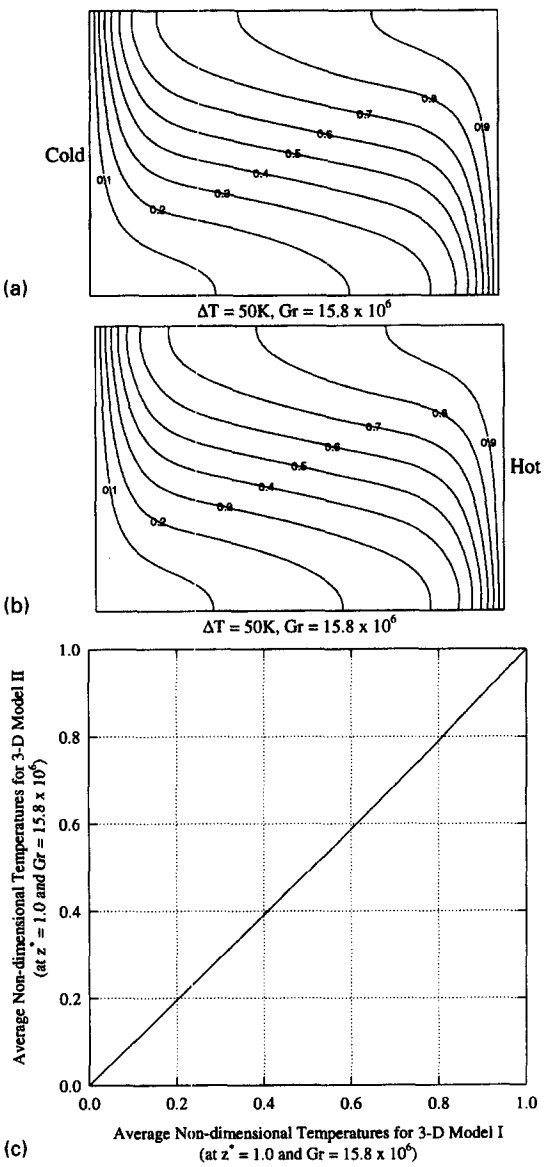

Fig. 5. Average nondimensional temperature contours. (a) Three-dimensional Model I. (b) Three-dimensional Model II. (c) Comparison of three-dimensional Model I vs three-dimensional Model II.

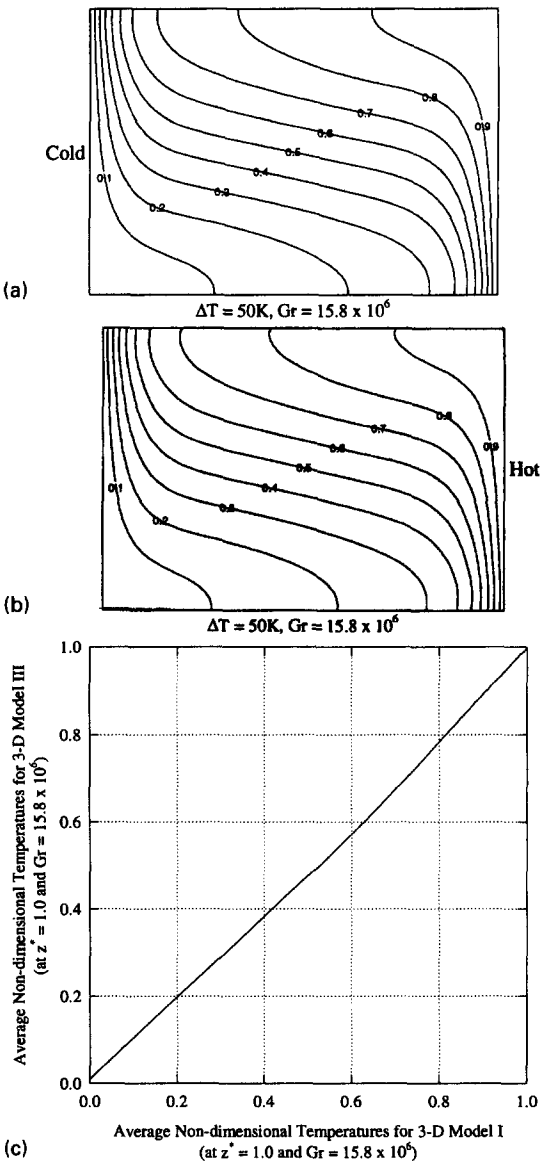

Fig. 6. Average nondimensional temperature contours. (a) Three-dimensional Model I. (b) Three-dimensional Model III. (c) Comparison of three-dimensional Model I vs three-dimensional Model III.

perature contour plots of the central plane and that of the average temperatures across 11 planes for three-dimensional Model III at $Gr = 15.8 \times 10^6$, respectively. These plots show that a difference does exist if we just consider the central plane only, as opposed to an average temperature across the width of the test cell.

Figure 7(c) is a comparison of the temperatures at the central plane to that of the average temperatures in the three-dimensional Model III at $z^* = 1.0$ and $Gr = 15.8 \times 10^6$. It can be seen that although there is a slight deviation from the straight line in this plot, it is not significant. Even though the experimental technique is an integrating technique, we need not average the calculated temperatures across the width of the test cell in order to get a better approximation to the experimental results. We can conclude that using the temperatures from the central plane of the fluid cavity is sufficient to get a good numerical solution to compare to the integrating X-ray radioscopy experimental image. However averaging may be necessary if one uses a cavity larger than the narrow gap cavity used in the present experiments.

Figure 8(a, b) shows the temperature contours for $Gr = 15.8 \times 10^6$ from the numerical simulation using three-dimensional Model III and the experimental radioscopic visualization, respectively (Koster *et al.* [7] described in detail the procedure used for obtaining the experimental radioscopic visualization image). These plots are color coded in black and white to simulate interferogram. For the same Grashof

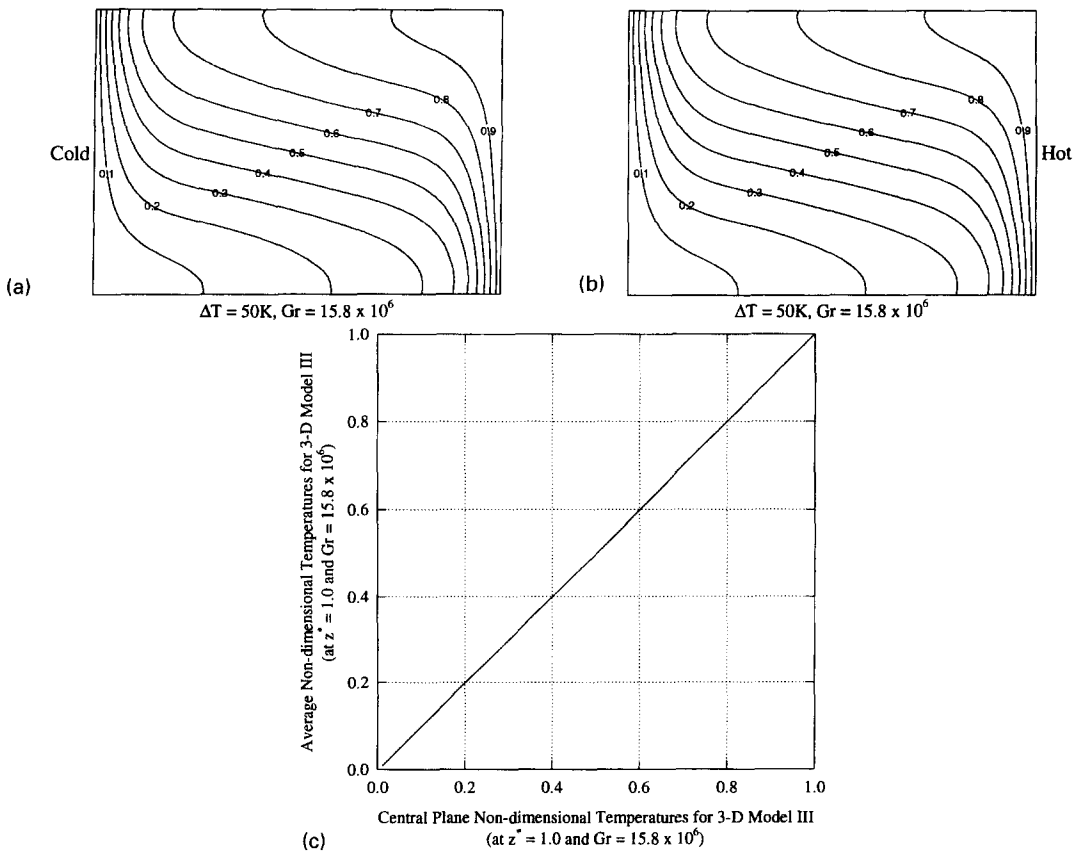

Fig. 7. Nondimensional temperature contours. (a) Central plane in the test cell cavity for three-dimensional Model III. (b) Average for the three-dimensional Model III. (c) Comparison of the central plane vs the average nondimensional temperatures for three-dimensional Model III.

numbers, the contour plots between the numerical simulation and the experimental image are in good agreement.

The experimental technique, however, is not as perfect as numerical simulation which is discussed by Koster *et al.* [7]. Listed below are a few limitations that exist when we try to compare the numerical results to the experimental results in the natural convection of gallium:

(1) A lead masking must be applied to the test cell, covering all parts except the cavity. This was necessary in order to prevent Bragg scattering from metal parts such as the thermodes. This masking reduces the field of view of the liquid layer by about 2 mm (~5%) of the cavity size. A loss of some information on all four sides of the liquid layer is the consequence.
(2) The X-ray beam is slightly divergent (4°). We did not simulate this radiation path in our numerical calculations.
(3) In the numerical modeling, we assumed adiabatic outer planes for the central volume that includes side walls and liquid layer. In the actual experiment this is not true due to heat losses.

8. CONCLUSIONS

Two- and three-dimensional modeling of steady natural convection in a narrow gap of a low Prandtl number pure liquid metal gallium was performed. Numerical simulation revealed that the temperature profiles obtained from the two-dimensional model differ significantly from those obtained in the three-dimensional models. Three different three-dimensional numerical models are compared to each other and to that of an experimental radioscopic visualization. With the inclusion of solid walls in the three-dimensional numerical model, the temperature contours were in good agreement with the experimental visualization. Using the temperature field of the central plane of the three-dimensional Model III is found to be sufficient to get a good numerical solution for comparison with the integrated experimental visualization of the temperature field in a narrow gap. The numerical modeling substantiates that solid walls with their finite heat conductivity play a very important part in liquid metal convective studies and cannot be neglected in numerical modeling.

Acknowledgements—Research support from NSF under

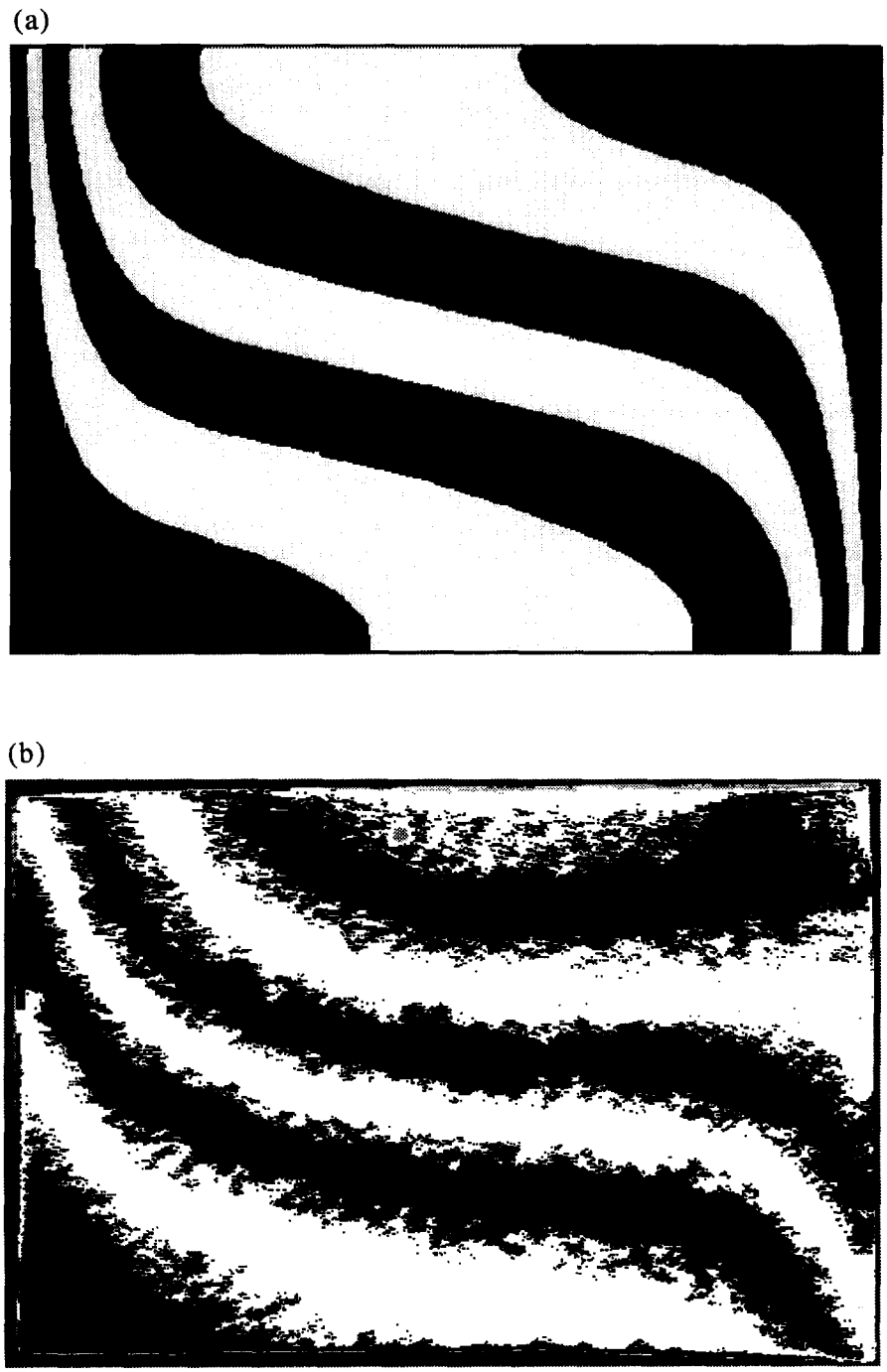

Fig. 8. Average temperature distribution in liquid gallium at $\Delta T = 50$ K and $Gr = 15.8 \times 10^6$. (a) Numerically simulated using three-dimensional Model III. (b) Experimentally determined.

grants CTS-8906846 and CTS-9114775 and from NASA under grant NCC3-210 is greatly appreciated. The authors would like to thank students Tom Campbell, Thomas Heusse and Martin Galmiche for their valuable discussions during the course of this modeling.

REFERENCES

1. P. G. Barber, R. K. Crouch, A. L. Fripp, W. J. Debnam, R. F. Berry and R. Simchick, A procedure to visualize the melt–solid interface in Bridgman grown germanium and PbSnTl, *J. Crystal Growth* **74,** 228–230 (1986).
2. K. Kakimoto, M. Eguchi, H. Watanabe and T. Hibiya, Direct observation by X-ray radiography of convection of molten silicon in the Czochralski growth method, *J. Crystal Growth* **88,** 365–370 (1988).
3. K. Kakimoto, M. Eguchi, H. Watanabe and T. Hibiya, *In-situ* observation of solid–liquid interface shape by X-ray radiography during silicon single crystal growth, *J. Crystal Growth* **91,** 509–514 (1988).

4. T. A. Campbell and J. N. Koster, Visualization of liquid/solid interface morphologies in gallium subject to natural convection, *J. Crystal Growth* **140,** 414–425 (1994).
5. T. A. Campbell and J. N. Koster, Radioscopic visualization of indium antimonide growth by vertical Bridgman–Stockbarger technique, *J. Crystal Growth* **147,** 408–410 (1995).
6. R. E. Pool and J. N. Koster, Visualization of density fields in liquid metals, *Int. J. Heat Mass Transfer* **37,** 2583–2587 (1994).
7. J. N. Koster, T. Seidel and R. Derebail, A radioscopic technique to study convective fluid dynamics in opaque liquid metals, *J. Fluid Mech.* (submitted).
8. M. J. Stewart and F. Weinberg, Fluid flow in liquid metals I. Theoretical analysis, *J. Crystal Growth* **12,** 217–227 (1972).
9. M. J. Stewart and F. Weinberg, Fluid flow in liquid metals II. Experimental observations, *J. Crystal Growth* **12,** 228–238 (1972).
10. R. Viskanta, D. M. Kim and C. Gau, Three-dimensional natural convection heat transfer of a liquid metal in a cavity, *Int. J. Heat Mass Transfer* **29,** 475–485 (1986).
11. F. Wolff, C. Beckermann and R. Viskanta, Natural convection of liquid metal in vertical cavities, *Expl Thermal Fluid Sci.* **1,** 83–91 (1988).
12. G. T. Murray and T. A. Lograsso, Properties of metals. In *Metals Handbook*—Vol. 2—*Properties and Selection: Nonferrous Alloys and Special-Purpose Materials* (Edited by ASM International Handbook Committee), pp. 1114–1115. ASM International, Metals Park, OH (1990).
13. G. F. Carter, Mechanical, physical and chemical properties of metals. In *Metals Handbook—Desk Edition* (Edited by H. E. Boyer and T. L. Gall), p. 2.19. American Society for Metals, Metals Park, OH (1984).
14. Lucite L, Cast acrylic sheet, *Basic Product Information.* DuPont Polymer Products, Wilmington, DE (1991).
15. ASM committee on definitions of metallurgical terms, Glossary of metallurgical terms and engineering tables. In *Metals Handbook—Desk Edition* (Edited by H. E. Boyer and T. L. Gall), pp. 1.44–1.45. American Society for Metals, Metals Park, OH (1984).
16. *FIDAP* 7.0—*Fluid Dynamics Analysis Package—Theory Manual,* Chap. 3. Fluid Dynamics International, Evanston, IL (1993).
17. W. Hauf and U. Grigull, Optical methods in heat transfer. In *Advances in Heat Transfer* (Edited by J. P. Hartnett and T. F. Irvine Jr), Vol. 6, pp. 133–366. Academic Press, New York (1970).